LASER & PHOTONICS REVIEWS

www.lpr-journal.org

Near-Zero Index Photonic Crystals with Directive Bound States in the Continuum

Larissa Vertchenko, Clayton DeVault, Radu Malureanu, Eric Mazur, and Andrei Lavrinenko*

Near-zero-index platforms arise as a new opportunity for light manipulation with boosting of optical nonlinearities, transmission properties in waveguides, and constant phase distribution. In addition, they represent a solution to impedance mismatch faced in photonic circuitry offering several applications in quantum photonics, communication, and sensing. However, their realization is limited to the availability of materials that could exhibit such low index. For materials used in the visible and near-infrared wavelengths, the intrinsic losses annihilate most of near-zero index properties. The design of all-dielectric photonic crystals with specific electromagnetic modes overcomes the issue of intrinsic losses while showing effective mode index near zero. Nonetheless, these modes strongly radiate to the surrounding environment, greatly limiting the devices applications. Here, a novel all-dielectric photonic crystal structure is explored that is able to sustain effective near-zero-index modes coupled to directive bound-states in the continuum in order to decrease radiative losses, opening extraordinary opportunities for radiation manipulation in nanophotonic circuits. Moreover, its relatively simple design and phase stability facilitate integration and reproducibility with other photonic components.

1. Introduction

The increasing demand for computational power, efficiency, and portability has boosted research in photonics engineering, where the study of materials and new ways to transmit information has become essential.[1] In particular, we see the rise of near-zero index materials and their influence on quantum technologies, promising to enable light manipulation for complex computational tasks.[2,3] Photonic chips are the predominant platform to create quantum computers, as well as sensors and communication devices.[4,5] The three main elements of such systems are sources of light, such as quantum dots, channels responsible for manipulating and transmitting information, and detectors in a phase-stable platform.[6] Each of these components must be designed taking into consideration their material, integration on-chip, and functionality. An outstanding challenge regarding photonic chips is the existence of high impedance mismatch between its components, limiting integration and resulting in high reflections and phase deterioration. Hybrid integration approaches incorporate different photonic fabrication technologies, which would not be achieved by a single fabrication process.[1] In this way, complex on-chip systems could be realized by integrating photon sources, waveguides, and detectors.

One way to overcome the impedance mismatch is by using materials with the refractive index close to zero, the so-called near-zero index materials (NZIM).[7] Inside these materials light will experience exotic phenomena, such as enlargement of the wavelength,[8] enhancement of nonlinearities,[9,10] high electric fields,[11] and constant phase distribution.[12] In particular, the constant phase related to a small wave vector leads to important applications in quantum photonics.[13,14] A large number of optical components integrated on chip can introduce multiple phase changes. When photons interact with such environment they acquire random phase distributions that will disrupt their signal, causing decoherence, hence losing its quantum properties.[15] Inside NZIM, radiation will be coherent due to the constant phase property, enabling us to perform operations in reasonable time before the information is lost. Moreover, low-index platforms exhibit impressive nonlinear efficiencies that would be otherwise achieved only by extremely intense laser sources. Its constant phase property also relaxes the phase-matching condition for several nonlinear effects, such as harmonic generation processes. As most materials exhibit low nonlinearities, NZIM becomes essential for many applications that rely on

Dr. L. Vertchenko
NanoPhoton – Center for Nanophotonics
Technical University of Denmark
Ørsteds Plads 345A, Kgs. Lyngby DK-2800, Denmark
E-mail: lariv@fotonik.dtu.dk
Dr. R. Malureanu, Prof. A. Lavrinenko
Technical University of Denmark
Ørsteds Plads 345A Kgs. Lyngby DK-2800, Denmark
Dr. C. DeVault, Prof. E. Mazur
Department of Physics and School of Engineering and Applied Sciences
Harvard University
9 Oxford Street, Cambridge MA 02138, USA

The ORCID identification number(s) for the author(s) of this article can be found under https://doi.org/10.1002/lpor.202000559

DOI: 10.1002/lpor.202000559

nonlinear optical phenomena, including data storage and quantum information.[9] Our research aims to provide a phase-stable component that could be integrated into hybrid photonic chips, with low coupling losses due to small impedance difference.

Conductors such as transition nitrides, ITO and other transparent conductive oxides have been studied for NZI properties. However, their intrinsic losses hinder their use for waveguiding applications, at the visible and near-infrared wavelengths.[16–18] The relative permittivity (ϵ) and permeability (μ) dictate how the charges of a medium will align to external electromagnetic fields and are related to the refractive index by $n = \sqrt{\mu\epsilon}$. Thus, in principle these materials would also behave as NZIM. However, the imaginary part of ϵ, which is associated with intrinsic losses, is overly high annihilating near-zero index effects in the system.[19] As a consequence, researchers are exploring ways to use dielectrics instead of conductors to achieve a near-zero regime without intrinsic losses.[20,21] It is well known that bulk dielectrics have refractive index above one. Periodically arranged dielectric structures are able to collectively excite resonances that might exhibit an effective mode index less than one. The Γ point lies at the center of the primitive cell in the reciprocal space (Brillouin zone), having a zero wave vector. By employing dielectric photonic crystals designed to support specific resonances[22] having accidental degeneracy at Γ, it is possible to attain an effective near-zero index mode.[23] For instance, Huang et al.[24] showed that silicon pillars, of radius r, arranged periodically with lattice constant $a = 2r$ would exhibit two linear bands and an additional flat band intersecting at a triply degenerate point. For the electric field oriented parallel to the cylinders axis, these three electromagnetic modes would correspond to two dipolar and a monopolar resonance. Close to the so-called Dirac's triple point the photonic crystal would be able to sustain an effective near-zero index, where both permittivity and permeability would be effectively near zero. In this way the wave impedance, given by $Z = \sqrt{\mu/\epsilon}$, would match the free space, allowing complete integration between sources, waveguides, and detectors.[25,26] Nonetheless, the modes excited in these structures are localized above the light-line, meaning that they easily couple to the environment, resulting in radiative losses.

Aiming to diminish leakage of radiation to the surroundings, several research groups[27–29] theoretically proposed near-zero index photonic crystals that could exhibit special resonances named bound states in the continuum (BICs).[30,31] Two classes of BICs may be explored in a system.[32] Symmetry-protected BICs are a result of a mismatch between the symmetry of modes in free space and the modes inside the system, occurring only at the Γ point.[32,33] Whereas trapped BICs are resonances in the system that collectively result in destructive interference outside the structure, preventing leakage of radiation.[34,35] Due to their non-radiative character, the Q-factor of BICs becomes infinite, meaning that radiation is completely confined in the system. In most BIC demonstrations, the out-of-plane absence of radiation is analyzed, while in-plane propagation happens in all allowed directions of the photonic crystal lattice. Nonetheless, there is a class of BIC, named separable BIC, where the direction of radiation can be manipulated in-plane, resulting in guided resonances while maintaining the out-of-plane fields inhibited. Its first confirmation was recently reported in a 1D photonic crystal trench.[33] Such guided resonances lead to important applications, such as control of radiation in energy-efficient photonic crystal lasers and photonic antennas. It is an enormous challenge to combine BICs with a NZIM, mainly due to difficulties in finding feasible shapes of the photonic crystals' unit cell. Furthermore, NZIM are highly dependent on polarization, thus complicating the overall process of discovering the right geometry. Recently, an experimental report[36] has tried to reproduce the theoretical results predicted by Minkov et al. claiming a NZI material with BIC. However, an analysis of the effective refractive index values that could sustain such claim was missing. In photonic circuitry, in-plane polarization (TE) is the preferable to work with, making the system of pillars previously suggested unfeasible for such polarization. Therefore, we investigated photonic crystal slabs made of silicon that would behave as NZIM and are able to contain separable BICs, at the near-infrared range.

Here we report the experimental characterization of a novel Si photonic crystal geometry. Our insight was that finding NZI materials with BIC modes for TE polarization on all-dielectric slabs demands complex structures inconvenient for fabrication.[27] In order to form an NZI material the degeneracy of the electromagnetic modes should be considered. A single simple shape of the unit cell that would give the right modes would be hard to find and probably optimization techniques would have to be employed. Our approach relies on simplifying the geometry by composing the unit cell with different circular holes radii, convenient for fabrication techniques. Furthermore, C_{4v} and C_{6v} symmetries give isotropic conical dispersions. Aiming to reach anisotropic Bloch modes for controlling the in-plane propagation direction of the BICs, an elliptical dispersion is needed. Consequently, by hybridizing triangular (C_{6v}) and square lattices (C_{4v}) with the different hole sizes, we were able to get the C_{2v} symmetry. The control of the modes for achieving the semi-Dirac point can be done by tuning both radii, as depicted in **Figure 1**a. The symmetry protected and accidental BICs can be reached by adjusting the final lattice constant afterwards. In our system, we were able to achieve conditions for a trapped BIC in the ΓX direction. Theoretical calculations of the Si membrane showed that such structure would be able to reach Q-factors as high as 10^{18}, which is normally found by concentrating light in optical cavities. The system was designed to have a BIC and Dirac degeneracy near the wavelength of $\lambda = 1550$ nm. The C_{2v} symmetry applied to the lattice in the x and y directions resulted in the first observation of a separable quasi-BIC in a 2D photonic crystal, where radiation was able to propagate only in one direction inside the slab (ΓX). We have performed transmission measurements leading to a Q-factor of 2546. Such discrepancy to theory can be explained by the finite size of the sample (400 μm × 400 μm), substrate presence (silica), limited equipment resolution, and natural fabrication imperfections, which naturally break the symmetric character of BICs, resulting in high, but finite Q-factors.[37] Nonetheless, our result is still high when compared to trivial photonic crystal membranes.[38] Our achievements pave the way to novel photonic crystal devices with high nonlinearities, light confinement, and constant phase distribution, as well as better integration due to near-zero index properties regarding impedance mismatch. Moreover, by exploring separable BICs we manage to have control over the light's propagation direction in-plane, finding important applications for optical switches and photonic circuitry.

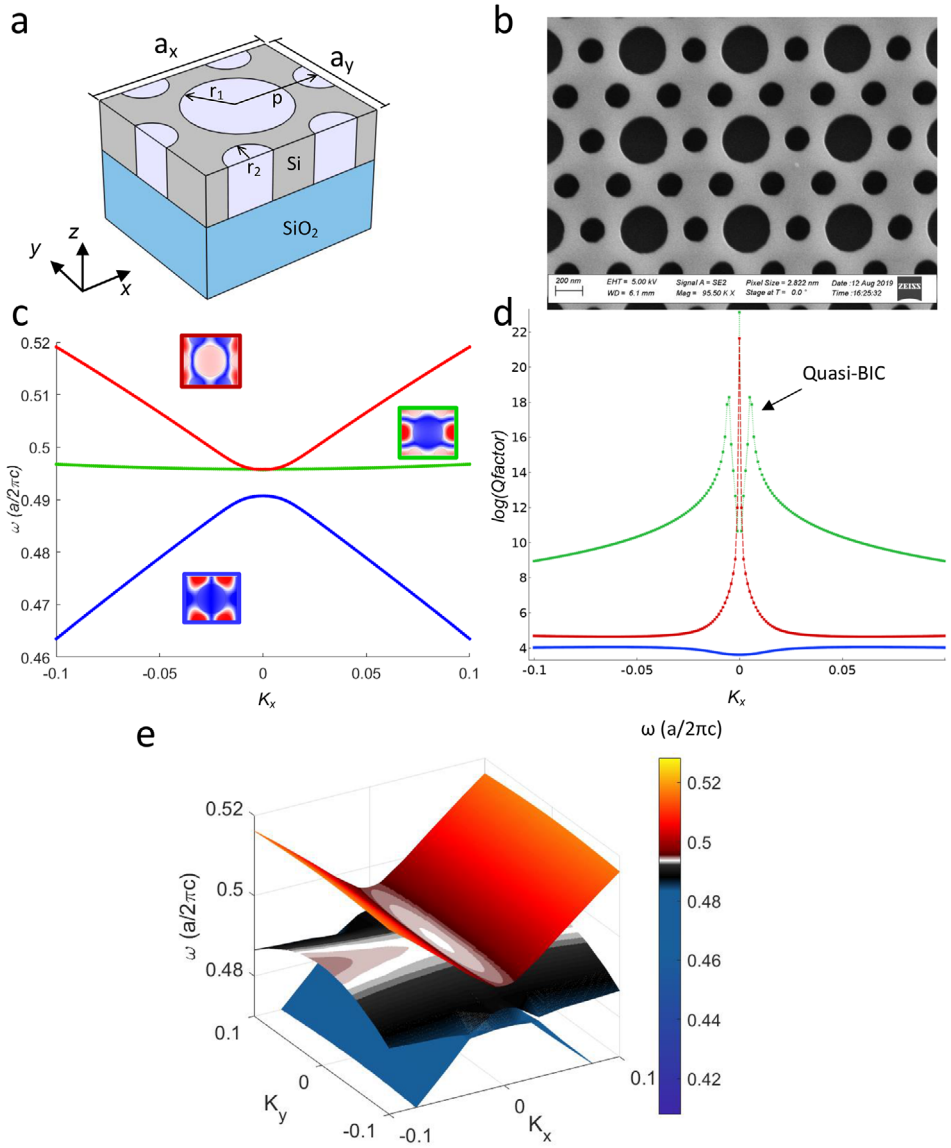

Figure 1. Fabricated structure and theoretical results. a) Unit cell of the proposed design for a Si slab on silica substrate, with air holes of radius 210 and 96 nm. b) SEM picture of a sample made of a 208 nm thick Si slab on silica substrate. c) 2D band structure of the system without substrate in the ΓX where the color scheme indicates the electromagnetic modes in the slab. d) Theoretical Q-factor for the proposed Si slab with hybrid air holes calculated along k_x through the equation $Q = \omega'/2\omega''$. e) Full band diagram of the slab as a function of ω, where the color scheme helps to identify the isofrequency profile.

2. Results

2.1. Material Choice and Fabrication Approach

The fabricated structure consists of a 208 nm thick Si slab with air holes of different radii r_1 and r_2, forming a flower-like shape pattern, as shown by the unit cell in Figure 1a. An amorphous Si (a-Si) was deposited on fused silica glass followed by electron-beam lithography and resist development. The a-Si was etched using a Bosch process with the resist as a mask (see "Experimental Section"). The air holes were designed to have a radius of $r_1 =$ 210 nm and $r_2 = 96$ nm, as depicted in the scanning electron microscopy (SEM) image in Figure 1b. The radial distance between the center of the biggest hole to the smaller ones is given by $p =$ 379 nm, which results in different lattice constants for the x and y directions ($a_x = 758$ nm $a_y = 656$ nm). Through numerical simulations using the "Wave optics" module with "Electromagnetic waves, frequency domain" physics in the commercially available software COMSOL,[39] we were able to retrieve the band diagram as well as the electromagnetic modes, for TE polarization, of the designed structure without the silica substrate, as shown in Figure 1c, as a function of the normalized angular frequency ω. In this first part, the silica was disregarded solely to analyze the properties of the structure without environmental influence. The full description of the computational method is presented in the Supporting Information. The influence of the substrate is considered

in the Experimental characterization section. The Si was modeled with a refractive index of 3.69, measured by ellipsometry for the wavelength of 1550 nm. From the dispersion diagram, we observed the same tendency for the combination of electromagnetic modes at the Dirac's triple point, where the color scheme indicates the different modes in the system. However, when the three modes intersect additional longitudinal waves are created due to radiation having electric field components aligned to the wave vector, disturbing the phase profile,[40] which would be uniform in a homogeneous near-zero index material. In this case, we decided to isolate the lower frequency mode (quadrupole) that would be responsible for such fluctuations. At the wavelength of 1536 nm, two modes intersect representing what is called a Semi-Dirac point,[41–43] which is created by the accidental degeneracy of two modes having a linear dispersion in one direction (k_x) and nonlinear relation in the perpendicular orientation (k_y). Close to $k = 0$, for the k_x direction, the medium will have the effective permittivity and permeability simultaneously near-zero ($\varepsilon_{\text{eff}} \approx 0$ and $\mu_{\text{eff}} \approx 0$), while for k_y it will behave as only an mu-near-zero (MNZ) material ($\varepsilon_{\text{eff}} \neq 0$ and $\mu_{\text{eff}} \approx 0$). These results give great possibilities to manipulate light propagation, such as optical switches, beam deflection and beam splitting.[40] So far, such system has not been experimentally reported in literature, being restricted to pillars working in the microwave range.[44]

Due to the linear behavior near the Γ point in the k_x direction, we were able to estimate the effective refractive index,n_{eff} of the electromagnetic mode for $\lambda = 1536$ nm according to the relation $n_{\text{eff}} = ck/\omega$, achieving a value of $n_{\text{eff}} = 0.02$. We also demonstrate the existence of a trapped quasi-BIC by studying the tendency of the Q-factor in Figure 1d, where it is possible to observe a local maximum displaced from Γ. By performing simulations of the photonic crystal with an eigenfrequency analysis,[39] we may determine the corresponding eigenvalues $\Omega = \omega' + \omega''$ of the structure. Therefore, we calculated the Q-factor of the system following $Q = \frac{\omega'}{2\omega''}$, where its peak determines the existence of a quasi-BIC with extremely high Q-factors of order 10^{18}. In principle, true BICs, i.e., modes with diverging Q factor, could be numerically achieved by tuning the hole dimensions with variation less than 1 nm (see Supporting Information). Such sensitivity to structural parameters can explain the discrepancy with the Q-factor measurements where it easily deteriorated to values in the order 10^3. Nonetheless, computational time and already imposed fabrication resolution (uncertainty of ±5 nm) do not justify such fine-tuning. Realistically, radiation and scattering losses cause all-dielectric platforms to have a slight quadratic dispersion at the intersection of the electromagnetic modes. This means that instead of a Dirac point, which is related to Hermitian systems, there is a ring of exceptional points. However, we will consider them equivalent since the ring radius is negligible as compared to the flat solutions in the dispersion diagram.

A full 3D image of the band structure is shown in Figure 1e, where the color scheme is used to evidence the isofrequency profile.

2.2. Experimental Characterization

The optical characterization of the fabricated structure consisted of two parts, visualization of isofrequency contours at the Fourier plane and transmission measurements for Q-factor retrieval.[33] In both cases a tunable laser source (Santec TSL-550) with a wavelength ranging from 1500 to 1630 nm was used, where a polarized laser beam is focused on the sample by a near-infrared 10× objective. A scheme of the setup is shown in **Figure 2**. In order to verify the wavelength of the near-zero index mode, we analyzed the isofrequency contours in the reciprocal space, by using the resonance-enhanced photon-scattering technique.[45,46] This approach relies on the fact that natural fabrication disorders scatter light not only at the resonance of interest, but also at different wave vectors close to it. All these resonances will radiate photons in the far field, which will then be projected into the Fourier plane by a 4f system, allowing us to reconstruct the isofrequency contour for various wave vectors. Since we need to interpret only the scattered signal that is directed towards the CCD camera, a second polarizer (P2) was used to block the reflected beam. In our setup, two 4f configurations (lenses L2-L5) were used to magnify the image onto the CCD. In particular lens L4 was used to switch from momentum space to real space, facilitating the alignment of the laser with the photonic crystal sample.

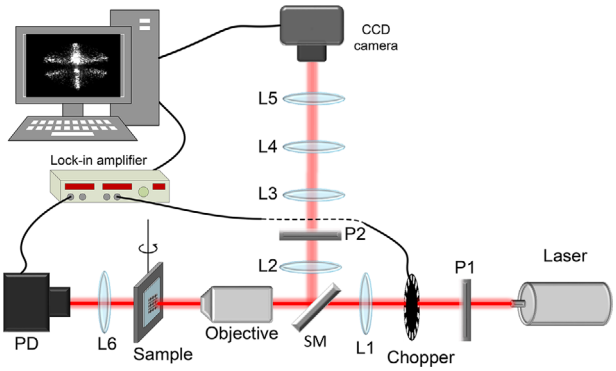

Figure 2. Experimental setup. Light from a tunable laser source is focused on the sample by an NIR objective. L1 (focal length $f = +15$ cm) is used to focus the beam onto the back focal plane of the objective. Lenses L2–L5 compose two 4f system to magnify and project the image into the Fourier plane. Polarizer P1 excites the right resonance in the sample, while P2 blocks the reflected signal so only the scattered field reaches the CCD camera. For transmission measurements, we use the phase-sensitive detection, where a 1 kHz chopper and the photodetector (PD) are connected to a lock in amplifier placed behind the sample. The full setup is integrated into a computer for data analysis.

By changing the laser's wavelength, we were able to visualize the isofrequency contour evolution and detect the wavelengths that corresponded to the degenerate points and quasi-BIC resonances. In **Figure 3**a, we make a comparison between the image captured by the CCD at the wavelength of the semi-Dirac point, 1536 nm, and theoretical simulations. We observed in the CCD picture three lines crossing, matching the theoretical prediction and proving the achievement of a NZIM. Apart from the semi-Dirac point wavelength, we were able to find two peculiar images of electromagnetic waves oriented along the y direction at 1527.5 and 1551 nm, as shown in Figure 3b. These field profiles are quasi-BICs, more precisely, they are called separable quasi-BICs,[47] due to their unidirectional character. Since BICs are characterized by their high Q-factor, which is related to confinement, they cannot be inferred solely by looking at the

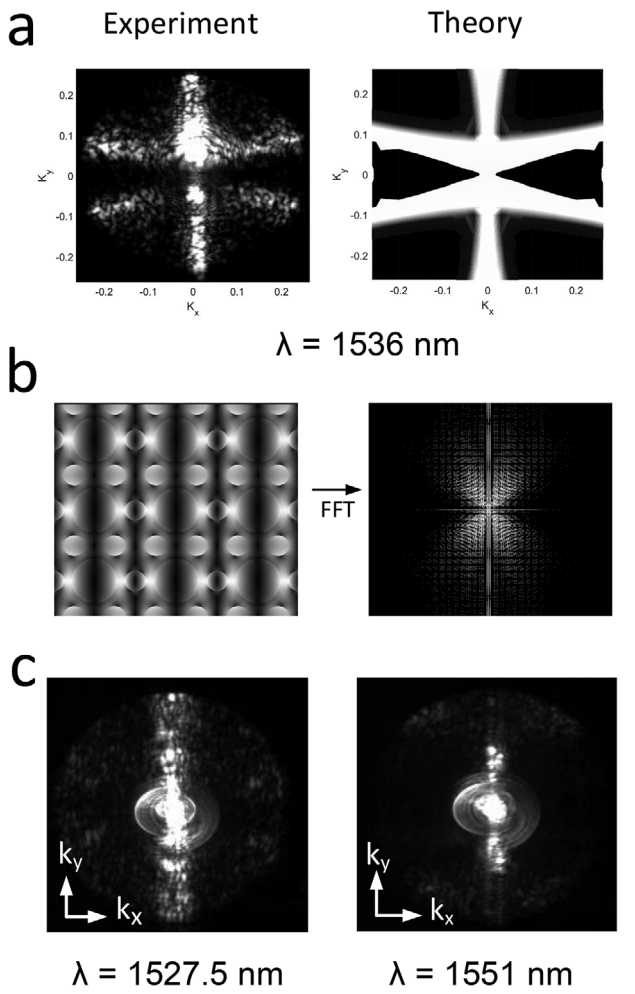

Figure 3. Isofrequency images of a semi-Dirac point and separable quasi BICs a) Isofrequency contour measured at the CCD camera (left) and obtained by numerical simulations (right), corresponding to the semi-Dirac point at the wavelength of 1536 nm. b) Isofrequency contour captured on the CCD camera for the separable quasi-BICs localized at the wavelengths 1527.5, 1551 nm. c) Theoretical prediction of the quasi-BIC profile by a Fourier transform of the electromagnetic mode of the unit cell at the BIC wavelength (1530 nm), taken from the simulation results.

band diagram. In Figure 3c we show the theoretical prediction of the quasi-BIC pattern in k-space by performing a Fourier transform on the mode profile of the unit cell region. Thus, the transmission experiment becomes necessary in order to retrieve the Q-factor curve of the structure.

When a system exhibits a BIC, the electromagnetic field is confined within at least one dimension. For instance, BICs in dielectric photonic crystal membranes will have vertical confinement. However, waves are still allowed to propagate in-plane, following the photonic crystal's band diagram. In our structure, the asymmetry applied in the photonic crystal lattice ($a_x \neq a_y$) represents another constraint in the system where no BIC exists in the k_y direction. In this case, the separable BIC will propagate in a single direction inside the slab, corresponding to the vertical straight lines we observed at the CCD in Figure 3b, for two different wavelengths (1527.5 and 1551 nm). These scattered field patterns are evidence of the coupling between quasi-BICs and Bloch waves in the photonic crystal environment.[48] Their validation was done by performing transmission measurements at the second part of the experiment. In the setup, light transmitted through the sample reaches a photodector (Thorlabs DET10C2), which is connected to a lock-in amplifier synchronized with a 1 kHz chopper placed in the path of the incoming beam, for the phase-sensitive detection. The lock-in amplifier will acquire the signal from the chopper and use it as a reference to process the input signal from the sample, minimizing possible extra noise sources. The transmission spectrum was normalized to the one measured without the structure, as depicted in **Figure 4**a, where it is possible to notice two thin dips highlighted in red. These dips represent the quasi-BICs around the semi-Dirac point wavelength, identified by the green line. Close to a quasi-BIC wavelength, narrow resonances (Fano resonances[49]) appear due to interference between the continuum resonant state and the discrete zero-index resonance. For each dip measured, we have fitted a Fano resonance curve and retrieved its Q-factor, according to $Q = f/\Delta f$, where f is the resonance frequency. The sample was attached to a rotation mount, where its angle was varied aiming to scan the q-factor for different wave vectors. The plots of the retrieved Q-factors as a function of the angle in respect to normal incidence are shown in Figure 4b,c. The first quasi-BIC observed (Figure 4b) at 1527.5 nm is near the wavelength measured for the semi-Dirac point (1536 nm) and its Q-factor value peaks around 3°, with a value 2546. This means that the quasi-BIC will also behave as an NZI mode, at such wavelength. Since the signature of such quasi-BIC is relatively small a better visualization of the first dip, by varying the angle of incidence is presented in the Supporting Information. A second quasi-BIC was observed at 1551 nm (Figure 4c) with Q-factor peaking around 2500. It is important to emphasize that the measured Q-factors have lower values than the ones calculated from the simulations mainly due to fabrication imperfections and the finite size of the sample (see Supporting Information). These values could be improved by making bigger samples or enhancing the system's symmetry by a full-suspended membrane, without any substrate.

In order to interpret the existence of two quasi-BICs around the semi-Dirac point, we numerically analyzed the band diagram of the fabricated structure including the dispersion of Si, retrieved from ellipsometry measurements. The permittivity plots for the Si slab may be found in the Supporting Information. Although the modes excited in the system are still the same, the inclusion of dispersion has shifted the semi-Dirac point from $k_x = 0$ to $k_x = 0.004$, as shown in **Figure 5**a. From this band structure, we have calculated the Q-factor, as depicted in Figure 5b. The results show that it is possible to observe two local maxima around the semi-Dirac point for the dipole mode, corresponding to the two quasi-BICs observed in the experiment. Deviations in wavelength from theoretical calculations are expected due to fabrication resolution and imperfections. For such reason, the semi-Dirac point, calculated at 1529 nm was measured at 1536 nm and the wavelength of the local maxima for the quasi-BICs also varied.

Since the degeneracy is no longer at the Γ point, the quadratic behavior of the dispersion becomes more pronounced imposing the question whether the effective parameters of the material remain near zero. In this sense, we have validated the

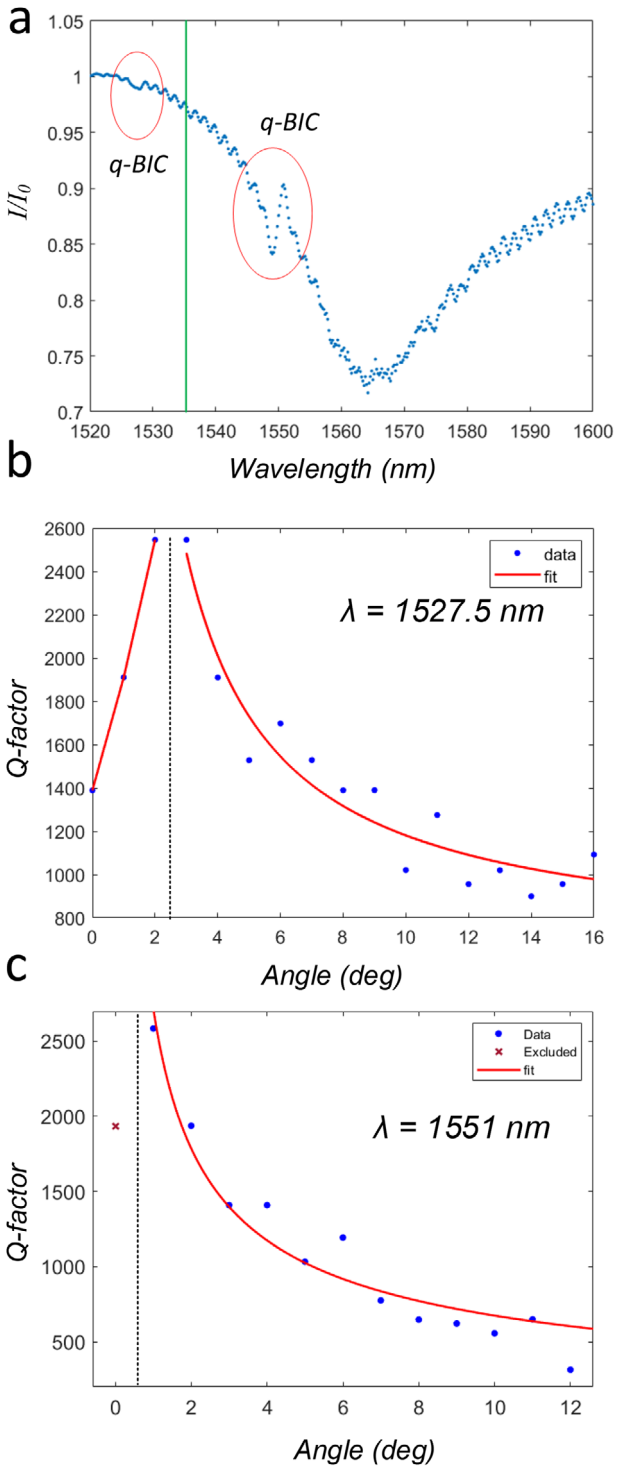

Figure 4. Transmission and Q-factor measurements a) Normalized transmission spectrum measured by the photodetector at normal incidence. The highlighted regions in red represent the first and second separable BICs, while the green line marks the Dirac's triple point wavelength (1536 nm).b,c) Q-factor plots as a function of the angles of the sample, where b) is the NZI quasi-BIC around 1527.5 nm and c) is another quasi-BIC related to dispersion. The red curves represent a rational fit, where the point for the lowest angle at c) was excluded due to a lack of data for a proper fitting.

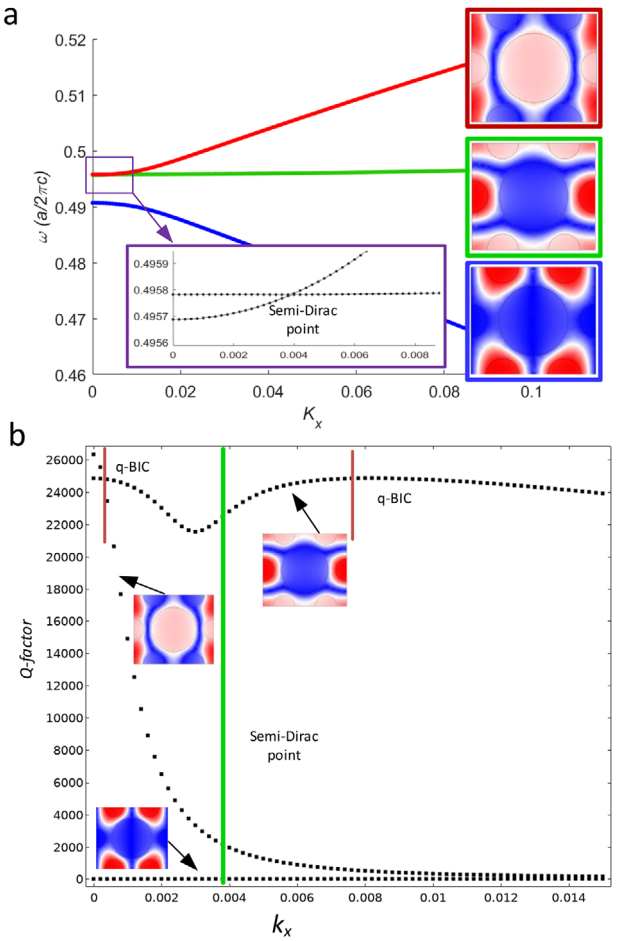

Figure 5. Dispersion diagram and Q-factor of the fabricated structures. a) Band structure with the respective electromagnetic mode profiles, considering Si dispersion. The highlighted region shows the shift of the semi-Dirac point from the center of Brillouin zone. b) Q-factor retrieved from the band diagram, where local maxima (red lines) indicate quasi-BICs around the semi-Dirac point, located at the green line.

near-zero index behavior of the photonic crystal slab by calculating its effective parameters using the boundary effective medium[50] approach and comparing our structures to a homogeneous medium. This method relies on evaluating the average eigenstate fields (E, H) on the boundaries of the unit cell and calculating the constitutive relations $D = \varepsilon E$ and $B = \mu H$, where the full mathematical description can be found in the Supporting Information. The retrieved effective permittivity $\varepsilon_{x\text{eff}}$ and $\varepsilon_{y\text{eff}}$ are shown in **Figure 6**, where the red line indicates the semi-Dirac point wavelength.

The C_{2v} symmetry of the unit cell results in an anisotropic medium, observed by the difference in the field profile when the slab is illuminated by a Gaussian beam with orthogonal polarization, as shown in **Figure 7**a. Such a system may be modeled as a homogeneous medium with previously computed effective parameters $\mu_{\text{eff}} = 0.0015$, $\varepsilon_{x\text{eff}} = 1.81$ and $\varepsilon_{y\text{eff}} = 0.16$, as depicted in Figure 7b. The simulations were performed by considering dipole sources localized in each unit cell of the structure, where we have calculated the magnetic field profile (H_z). As a conse-

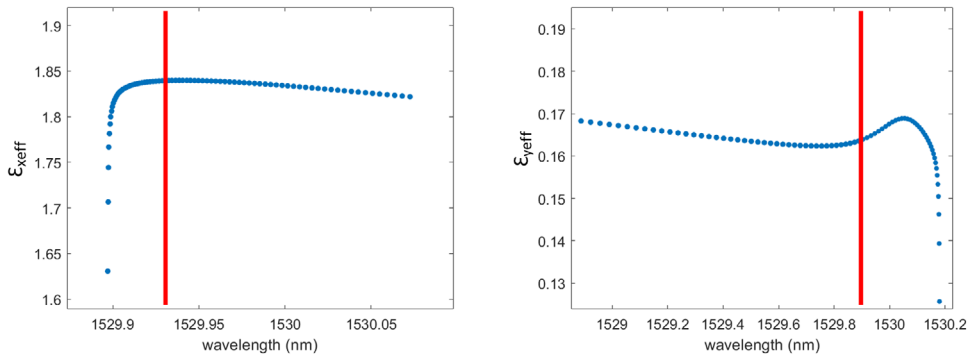

Figure 6. Permittivity retrieval. Plots of the retrieved effective permittivity ε_{xeff} and ε_{yeff} as functions of wavelength. The vertical line marks the semi-Dirac point wavelength.

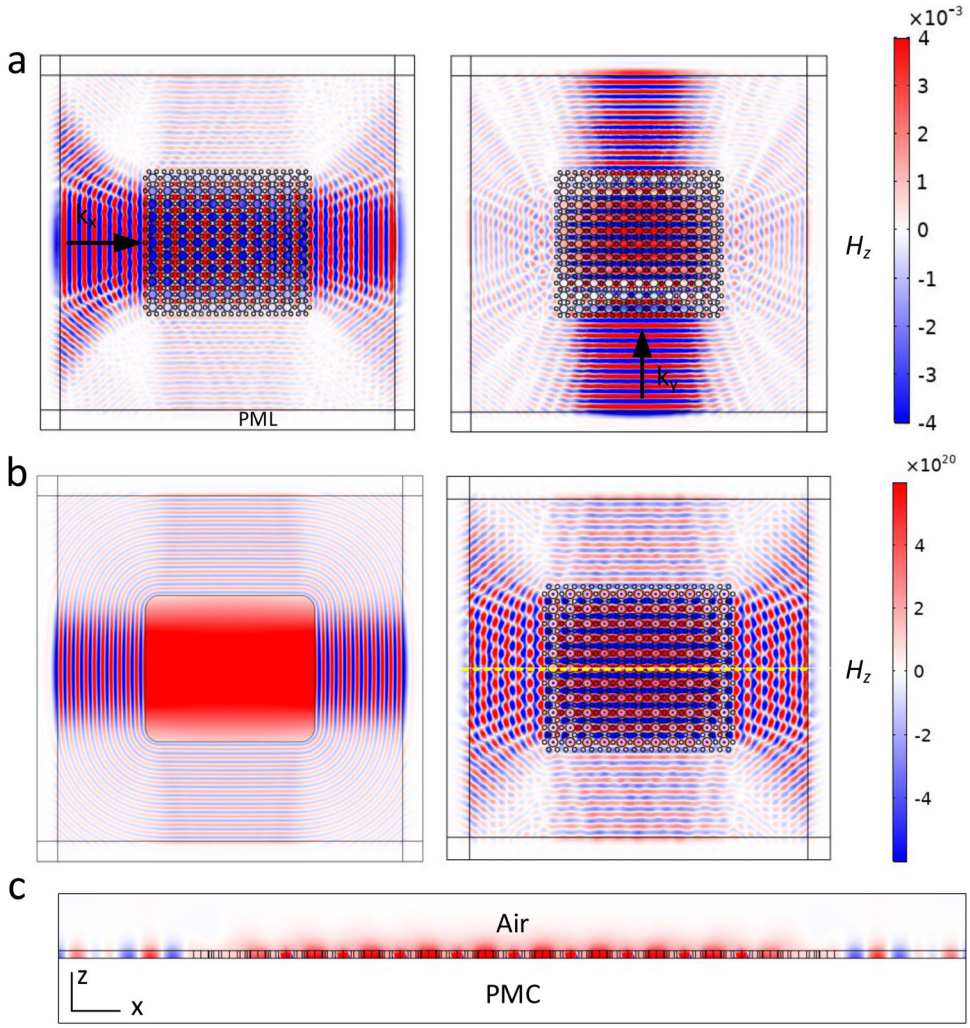

Figure 7. Effective refractive index and field profiles a) Magnetic field profile of the Si slab illuminated by a Gaussian beam with orthogonal orientation, with wave vector indicated by the arrows. b) Comparison between a homogeneous structure (left) with effective parameters parameters $\mu_{eff} = 0.01$, $\varepsilon_{xeff} = 1.81$ and $\varepsilon_{yeff} = 0.16$ and the fabricated structure (right), where the electromagnetic modes were excited by dipole sources. c) Quasi-BIC at the wavelength of 1527 nm, where the transverse field profile was taken at the yellow dashed line. By using symmetry considerations for TE modes the perfect magnetic conductor was applied to decrease computational demand.

quence of the finite size of the sample, edge effects will be more pronounced for the photonic crystal. In Figure 7c we plot the transverse profile of H_z in the XZ plane for a mode close to the semi-Dirac point, at 1527 nm, where we notice a high confinement of the radiation, equivalent to a quasi-BIC regime. As expected from a near-zero index material, the phase of all elementary cells is constantly leading to the wavefront shaping property, where an incoming electromagnetic wave is able to excite plane waves at the outgoing interfaces. Therefore, we were able to confirm the low-index property of our structure with effective refractive indexes equivalent to $n_{x\text{eff}} = 0.05$ and $n_{y\text{eff}} = 0.02$.

3. Discussion

We have experimentally verified the possibility to create a dielectric near-zero index material from a novel photonic crystal design of hybrid air holes in a Si slab. The effective refractive indices calculated for such structure were $n_{x\text{eff}} = 0.05$ and $n_{y\text{eff}} = 0.02$, which are unachieved by other platforms such as multilayers and homogeneous conductors, due to their intrinsic losses. By retrieving the isofrequency contour images of the structures, we were able to identify their effective NZI wavelength, corresponding to 1536 nm. Furthermore, we show that our structures are able to sustain a separable quasi-BIC helping to prevent radiative losses from the system while controlling the in-plane propagation direction of radiation. We have measured Q-factors as high as 2546 for the fabricated device. Although higher Q-factor values have been reported in literature for symmetric systems, we emphasize these results were obtained with glass as a substrate, which already deteriorates confinement. Better values could be reached by using self-standing membranes and a bigger area of the photonic crystal.

From the experimental results, we analyzed the effective constitutive parameters of the photonic crystal, validating its near-zero index property. Furthermore, the anisotropy of the quasi-BIC imposed by semi-Dirac cones due to C_{2v} rotation symmetry opens new possibilities for wave manipulation. Our hybrid structure of different circular holes greatly simplifies fabrication procedures. Such materials could pave the way for new structures in photonic crystal platforms, offering high electric field confinement, enhancement of nonlinearities, and phase-stable environments.

4. Experimental Section

Fabrication Process: In order to obtain the structures with the desired characteristics, the samples were fabricated in a class 100 cleanroom facility. In a first instance, amorphous Si (a-Si) was deposited on fused silica glass using LPCVD furnaces at 560 degrees centigrade to ensure an amorphous and not a poly-crystalline structure of the deposited Si. The first deposition was used to determine the deposition rate and the refractive index using ellipsometry techniques. Once the deposition rate and the refractive index was known, the data was used for a quick numerical simulation to determine the thickness of the Si layer. A second deposition was then performed to obtain the desired thickness. After the second deposition, the obtained thickness and refractive index were measured. These final data were then used for a full simulation and readjustment of the structure's dimensions. 150 nm e-beam resist on the sample was spun and then thermally deposited 20 nm Al. This was done in order to avoid charging effects during electron-beam lithography. After the exposure, the Al layer was removed using standard wet-etching in H_3PO_4: H_2O solution. One has then proceeded with developing the resist. The a-Si was etched using a Bosch process with the resist as mask. The selectivity between the resist and the a-Si is 1:7. The remaining resist was then removed using an O_2 plasma. Since the LPCVD furnace deposits on both sides of the wafer, the last fabrication step was a dry isotropic etch of the bottom Si using SF_6 plasma.

Numerical Modeling: FEM simulations were performed using the commercial software COMSOL Multiphysics. The structure was modeled using the unit cell of Figure 1a with Floquet periodic boundary conditions and perfectly matched layers at the top and bottom. The refractive index of Si used in the simulations was retrieved by ellipsometry measurements. Calculations of the band diagram and q-factors were performed by an eigenfrequency study.

Supporting Information

Supporting Information is available from the Wiley Online Library or from the author.

Acknowledgements

This work was supported by the Danish National Research Foundation through NanoPhoton - Center for Nanophotonics, grant number DNRF147. R.M. acknowledges the support of DTU Nanolab for the fabrication of the structures. A.L. acknowledges the support from the Independent Research Fund Denmark, DFF Research Project 2 "PhotoHub" (8022-00387B), Villum Fonden. The Harvard University team acknowledges support from DARPA under contract URFAO: GR510802.

Conflict of Interest

The authors declare no conflict of interest.

Author Contributions

L.V. carried out the simulations and designed the samples. R.M. fabricated the samples. L.V., C.D., and R.M. carried out the measurements. A.L. and E.M. supervised the research. All authors participated in the revision process of the manuscript.

Data Availability Statement

The data that support the findings of this study are available from the corresponding author upon reasonable request.

Keywords

bound states in the continuum, near-zero index materials, photonic crystals

Received: December 8, 2020
Revised: March 19, 2021
Published online: May 24, 2021

[1] J. H. Kim, S. Aghaeimeibodi, J. Carolan, D. Englund, E. Waks, *Optica* **2020**, *7*, 291.

[2] T. D. Ladd, F. Jelezko, R. Laflamme, Y. Nakamura, C. Monroe, J. L. O'Brien, *Nature* **2010**, *464*, 45.
[3] I. L. Chuang, R. Laflamme, P. W. Shor, W. H. Zurek, *Science* **1995**, *270*, 1633.
[4] S. Bogdanov, M. Shalaginov, A. Boltasseva, V. M. Shalaev, *Opt. Mater. Express* **2017**, *7*, 111.
[5] N. C. Harris, D. Bunandar, M. Pant, G. R. Steinbrecher, J. Mower, M. Prabhu, D. Englund, *Nanophotonics* **2016**, *5*, 456.
[6] A. W. Elshaari, W. Pernice, K. Srinivasan, O. Benson, V. Zwiller, *Nat. Photonics* **2020**, 14, 285.
[7] I. Liberal, N. Engheta, *Nat. Photonics* **2017**, *11*, 149.
[8] M. Silveirinha, N. Engheta, *Phys. Rev. Lett.* **2006**, 97, 157403.
[9] O. Reshef, I. De Leon, M. Z. Alam, R. W. Boyd, *Nat. Rev. Mater.* **2019**, *4*, 535.
[10] L. Caspani, R. P. M. Kaipurath, M. Clerici, M. Ferrera, T. Roger, J. Kim, A. Boltasseva, *Phys. Rev. Lett.* **2016**, *116*, 233901.
[11] I. Liberal, N. Engheta, *Sci. Adv.* **2016**, *2*, e1600987.
[12] L. Vertchenko, N. Akopian, A. V. Lavrinenko, *Sci. Rep.* **2019**, *9*, 6053.
[13] S. A. Biehs, G. Agarwal, *Phys. Rev. A* **2017**, *96*, 022308.
[14] R. Sokhoyan, H. A. Atwater, *Opt. Express* **2013**, *21*, 32279.
[15] H. J. Kimble, *Nature* **2008**, *453*, 1023.
[16] A. Boltasseva, H. A. Atwater, *Science* **2011**, *331*, 290.
[17] G. V. Naik, J. L. Schroeder, X. Ni, A. V. Kildishev, T. D. Sands, A. Boltasseva, *Opt. Mater. Express* **2012**, *2*, 478.
[18] M. Z. Alam, I. De Leon, R. W. Boyd, *Science* **2016**, *352*, 795.
[19] L. Vertchenko, L. Leandro, E. Shkondin, O. Takayama, I. V. Bondarev, N. Akopian, A. V. Lavrinenko, *Opt. Mater. Express* **2019**, *9*, 2117.
[20] S. Kita, Y. Li, P. Camayd-Muñoz, O. Reshef, D. I. Vulis, R. W. Day, M. Lončar, *Opt. Express* **2017**, *25*, 8326.
[21] D. I. Vulis, O. Reshef, P. Camayd-Muñoz, E. Mazur, *Rep. Prog. Phys.* **2018**, *82*, 012001.
[22] Q. Zhao, J. Zhou, F. Zhang, D. Lippens, *Mater. Today* **2009**, *12*, 60.
[23] J. Mei, Y. Wu, C. T. Chan, Z. - Q. Zhang, *Phys. Rev. B* **2012**, *86*, 035141.
[24] X. Huang, Y. Lai, Z. H. Hang, H. Zheng, C. Chan, *Nat. Mater.* **2011**, *10*, 582.
[25] D. I. Vulis, O. Reshef, P. Muñoz, S. Kita, Y. Li, M. Lončar, E. Mazur, in *Nano-Optics: Principles Enabling Basic Research and Applications* (Eds: B. Di Bartolo, J. Collins, L. Silvestri), Springer, Dordrecht, Netherlands **2017**, pp. 473–474.
[26] A. M. Mahmoud, N. Engheta, *Nat. Commun.* **2014**, *5*, 5638.
[27] M. Minkov, I. A. Williamson, M. Xiao, S. Fan, *Phys. Rev. Lett.* **2018**, *121*, 263901.
[28] L. Li, J. Zhang, C. Wang, N. Zheng, H. Yin, *Phys. Rev. A* **2017**, *96*, 013801.
[29] F. Monticone, H. M. Doeleman, W. Den Hollander, A. F. Koenderink, A. Alù, *Laser Photonics Rev.* **2018**, *12*, 1700220.
[30] C. W. Hsu, B. Zhen, A. D. Stone, J. D. Joannopoulos, M. Soljacic, *Nat. Rev. Mater.* **2016**, *1*, 16048.
[31] B. Zhen, C. W. Hsu, L. Lu, A. D. Stone, M. Soljacic, *Phys. Rev. Lett.* **2014**, *113*, 257401.
[32] Z. Sadrieva, K. Frizyuk, M. Petrov, Y. Kivshar, A. Bogdanov, *Phys. Rev. B* **2019**, *100*, 115303.
[33] X. Yin, J. Jin, M. Soljacic, C. Peng, B. Zhen, *Nature* **2020**, *580*, 467.
[34] A. Cerjan, C. W. Hsu, M. C. Rechtsman, *Phys. Rev. Lett.* **2019**, *123*, 023902.
[35] Y. Yang, C. Peng, Y. Liang, Z. Li, S. Noda, *Phys. Rev. Lett.* **2014**, *113*, 037401.
[36] H. Tang, C. DeVault, P. Camayd-Muñoz, Y. Liu, D. Jia, F. Du, E. Mazur, *Nano Lett.* **2021**, *21*, 914.
[37] R. Gansch, S. Kalchmair, P. Genevet, T. Zederbauer, H. Detz, A. M. Andrews, W. Schrenk, F. Capasso, M. Lončar, G. Strasser, *Light: Sci. Appl.* **2016**, *5*, e16147.
[38] L. Kassa-Baghdouche, T. Boumaza, E. Cassan, M. Bouchemat, *Optik* **2015**, *126*, 3467.
[39] COMSOL Multiphysics, COMSOL AB,Stockholm, Sweden. http://www.comsol.com **2020** (accessed: March 31, 2021).
[40] A. Mahmoud, I. Liberal, N. Engheta, *Opt. Mater. Express* **2017**, *7*, 415.
[41] U. G. Yasa, U. Gorkem, N. Eti, H. Kurt, Manipulation of light using semi-Dirac dispersion in low-symmetric photonic crystals. in *18th International Conference on Transparent Optical Networks (ICTON)*. IEEE, Piscataway, NJ, **2016**, pp. 1–4.
[42] X. T. He, Y. N. Zhong, Y. Zhou, Z. C. Zhong, J. W. Dong, *Sci. Rep.* **2015**, *5*, 1.
[43] L. Vertchenko, R. Malureanu, C. DeVault, E. Mazur, A. Lavrinenko, Low Index Asymmetric Bound States in the Continuum for Low Loss Integrated Photonics. In CLEO: Science and Innovations (pp. SM1J-2). Optical Society of America.
[44] U. G. Yasa, M. Turduev, I. H. Giden, H. Kurt, *Phys. Rev. B* **2018**, *97*, 195131.
[45] J. Jin, X. Yin, L. Ni, M. Soljačić, B. Zhen, C. Peng, *Nature* **2019**, *574*, 501.
[46] E. C. Regan, Y. Igarashi, B. Zhen, I. Kaminer, C. W. Hsu, Y. Shen, J. D. Joannopoulos, M. Soljačić, *Sci. Adv.* **2016**, *2*, e1601591.
[47] N. Rivera, C. W. Hsu, B. Zhen, H. Buljan, J. D. Joannopoulos, M. Soljačić, *Sci. Rep.* **2016**, *6*, 33394.
[48] G. Zito, S. Romano, S. Cabrini, G. Calafiore, A. C. De Luca, E. Penzo, V. Mocella, *Optica* **2019**, *6*, 1305.
[49] B. Luk'yanchuk, N. I. Zheludev, S. A. Maier, N. J. Halas, P. Nordlander, H. Giessen, C. T. Chong, *Nat. Mater.* **2010**, *9*, 707.
[50] Y. Wu, *Opt. Express* **2014**, *22*, 1906.